High-Speed PIV: Applications in Engines and Future Prospects

David Towers and Catherine Towers

School of Mechanical Engineering, University of Leeds, Leeds, LS2 9JT, UK
d.p.towers@leeds.ac.uk

Abstract. In this chapter we present the development of a high-speed imaging system for the measurement of automotive in-cylinder flows and sprays. High-speed imaging devices with framing rates of 12 000 images per second or more produce engine data at a resolution of at least one crank angle degree crankshaft rotation with engine speeds of up to 2000 rpm. In combination with high repetition rate pulsed lasers synchronized with the camera it is shown that data on liquid-fuel distribution can be obtained and analyzed. With the introduction of artificial tracer particles and appropriate data-processing techniques planar vector fields are obtained at the same temporal resolution. For both the spray and flow image sequences the data is considered as 4-dimensional: two spatial axes in the measurement volume, one temporal axis within an engine cycle and a further temporal axis from one engine cycle to another. A statistical analysis of the data produces information on the cyclic variability of the spray and flow fields that are critical to modern combustion system design. Whilst a high volume of information can readily be created, the industrial requirements are for validation of computational models or to provide insight into the mixture-preparation mechanisms as a means of evolving the design process. Therefore, an emphasis of this chapter is to show how the large quantities of detailed optical measurement data may be reduced in such a way as to pass on the most significant performance data to powertrain specialists.

1 Introduction

Automotive combustion remains a challenging area of research owing to increasingly strict emissions legislation coupled with ever more demanding consumer performance requirements. To make progress requires an increased understanding of combustible-mixture preparation, the combustion process itself and the formation of emissions. The ensemble-average development of the in-cylinder flow field and the breakdown of bulk flow features into turbulence during the compression stroke are known to affect burn rates. In addition to considering the temporal development of the flow field averaged over many engine cycles, the presence of cyclic variations in the bulk flow can critically affect combustion performance [1, 2]. The affect of cyclic variability on combustion is amplified in direct-injection combustion, e.g., gasoline direct injection (GDI), as the flow governs fuel transport as well as the conditions for flame propagation.

A. Schroeder, C. E. Willert (Eds.): Particle Image Velocimetry,
Topics Appl. Physics **112**, 345–361 (2008)

There are three primary sources of information that form the basis for combustion system development: thermodynamic engines, computational fluid dynamics (CFD) and optical diagnostics. Each source provides unique information. Thermodynamic engines provide overall system-performance data and critically enable engine emissions to be quantified accurately. However, no information is obtained on the detailed mechanism of mixture preparation or combustion. Reynolds-averaged CFD codes potentially provide full 3-dimensional data on all fluid properties and are resolved through the engine cycle. Furthermore, the development of large eddy and direct numerical simulations offer the potential to examine cyclic variability effects. However, appropriate validation remains a concern particularly when trying to incorporate spray and combustion models. Optical diagnostics based on particle imaging (Mie scattering) provide both qualitative and quantitative information on spray development and in-cylinder flow. Spectroscopic techniques offer the potential for postignition and species-specific measurements, e.g., of trace-gas production. It has been demonstrated that appropriate optical engines can be designed that reproduce the geometry and compression ratio of thermodynamic engines. The major differences between thermodynamic and optical engines are in the heat-transfer rates and in the piston rings used, depending on whether the rings run on the glass barrel, as is the case for full-stroke optical access, or whether the rings run on a metal barrel below a small length of optical barrel giving access only to the top end of the stroke. In either case, the crevice volume is normally slightly increased. With modern lasers and detectors, information at high temporal and spatial resolution is available for validation of computational models, to correlate with the performance of equivalent geometry thermodynamic engines or to be used directly within the combustion development process.

In this chapter we focus on techniques based on Mie scattering for imaging sprays and artificial tracer particles added to the flow field to enable 2-dimensional flow-velocity mapping through particle image velocimetry (PIV). The measurement of single vector fields in engines by PIV has been achieved for some time initially in a plane parallel to the head gasket [3] and subsequently imaging a bore centerline plane via a corrective optic to remove the distortion generated in imaging through a glass barrel [4]. However, the characterization of cyclic variability and turbulence in in-cylinder flows is not routine. Cyclic variability was quantified initially from single-point laser Doppler anemometry data [1] utilizing the time series of information produced and temporal filtering to isolate the high-frequency turbulence from the bulk-flow components. However, single-point techniques measuring one or two components of the velocity vector are very time consuming to apply for planar or volumetric mapping in an engine, particularly when a range of operating conditions need to be compared. Full-field approaches such as PIV and particle tracking velocimetry (PTV) offer the opportunity to break through the data-acquisition bottleneck, significantly reducing rig test time and transferring the issue to time-efficient data processing. However, single snapshots

of the velocity vector field as obtained from a typical double-frame PIV camera are not sufficient to separate the cyclic variability in a particular engine cycle from the turbulence in that cycle as a time series of information is traditionally needed for such an analysis. Initial attempts at achieving a full-field analysis of cyclic variability in engines was made in water-analogy rigs operating at a speed that was compatible with the cameras available at the time [5]. More recently, the use of higher-speed PIV systems, operating at image rates of a few 100 Hz have been used in conjunction with proper orthogonal decomposition to enhance the temporal resolution [6].

The work presented in this chapter concerns the quantification and data reduction of cyclic variability information in spray structure and planar velocity fields obtained from high-speed imaging in a single-cylinder optically accessed engine. The work is an expansion of a previous paper concerning enhanced data-processing techniques to give high validation rates in the PIV data obtained such that an automatic analysis of cyclic variability was possible [7]. Here, we include cyclic variability processing of high-speed Mie scattering images of direct injection gasoline sprays and examine the potential impact of recent developments in laser and camera hardware on the data obtainable from high-speed PIV in engines.

2 Experimental Systems

2.1 Optical Setup

The high-speed imaging equipment used in the experiments consisted of a Kodak 4540 CCD camera and 20 W average power copper-vapour laser. These hardware items are straightforwardly synchronized using the camera to define a pulse train sent to the laser to produce a pulse at the start of each camera frame. The useful framing rates available are 4.5, 9 and 13.5 kHz with spatial resolutions of 256×256, 256×128 and 128×128 pixels, respectively. The higher framing rates have been used herein and give an image and therefore pulse separation of approximately 111 and 74 μs. The disadvantage of this arrangement is that the interframe time and pulse separation for crosscorrelation analysis are always equal. Consequently, for the typical fields of view used in these experiments the PIV system has an upper velocity limit of approximately $20\,\mathrm{m\,s^{-1}}$ corresponding to a maximum particle displacement of ~ 4 pixels with 16-pixel interrogation regions used for crosscorrelation analysis. The upper velocity limit means that the system is compatible with in-cylinder flows from inlet valve closure through to the end of the compression stroke at engine speeds up to 2000 rpm. A further consequence of the long pulse separation coupled with the highly 3-dimensional nature of the flow field means that relatively thick, 1 to 2 mm, laser lightsheets must be used to increase the probability of exposing the same particles in consecutive frames. Out-of-plane motion was the primary cause of poor quality crosscorrelation

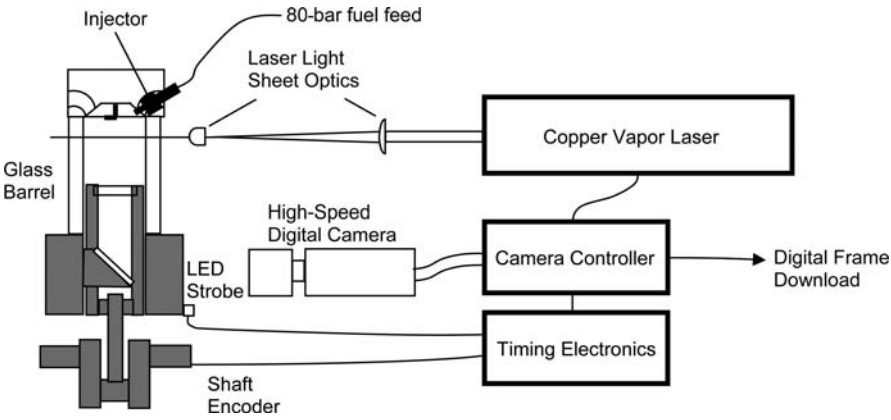

Fig. 1. Schematic representation of the optical system and engine

results from these experiments with the maximum out-of-plane displacement exceeding the design guidelines derived from previous Monte Carlo simulations [8]. It was found to be beneficial to use short focal length lenses to form the laser sheet in order to expand the beam quickly through narrow access points in order to illuminate the desired plane in the measurement volume. A typical schematic of the setup is given in Fig. 1.

2.2 Optical Engine

The optical engine used a production geometry 4-valve cylinder head and operated at a compression ratio of 11 : 1. Optical access was provided by a full-stroke fused-silica barrel and a window within the engine piston crown. The piston itself is elongated with one set of piston rings at the top running on the optical barrel and a further set of rings at the bottom running in a conventional metal barrel. A slot is machined into the piston body to enable a fixed mirror to be mounted directly beneath the piston crown optical window such that planes parallel to the head gasket can be imaged, see Fig. 1. The engine was operated at speeds up to 2000 rpm with run time limited to ~ 30 s due to temperature build up in the piston rings running on the optical barrel. Lubrication was not used between the rings and the barrel in order to prevent optical distortions in either the laser lightsheet or the images obtained. The engine incorporated a prototype hollow-cone fuel injector running from a fuel rail maintained at 80 bar via a camshaft-driven rotary fuel pump with the injector tip positioned in the combustion chamber between the inlet valves. The piston crown incorporated a bowl, slightly greater than half the cylinder bore diameter, designed to guide the directly injected spray towards the spark plug.

The engine timing was monitored using a crankshaft encoder and custom timing electronics provided crank-angle-resolved triggers for the fuel-injection system and high-speed camera. To provide a direct crank-angle reference in the captured image sequences an LED was mounted at the edge of the image field and triggered at a defined point within every engine cycle.

2.3 Seed-Particle Selection

The compromise in pulse separation and hence laser lightsheet thickness coupled with the available pulse energy of $\sim$ 2–3 mJ mean that conventional oil seeding cannot be satisfactorily imaged. Therefore, larger hollow microspheres were employed as a seeding material, Expancel 551 DE 40 from [9]. The thin-shelled particles had a mean diameter of 35 micrometers and a specific gravity of $\sim$ 0.04 giving a 95 % amplitude flow-following accuracy for a 1-kHz flow fluctuation rate in air at standard pressure and temperature, from [10]. This fluctuation rate corresponds to a swirl ratio of 30 in an engine operating at 2000 rpm, which is approximately a factor of 3 higher than that in typical GDI engines. In addition, the flow-following ability improves during the compression stroke owing to the increase in fluid density and viscosity. Care was needed in using the acrylonitrile microballoons to minimize the buildup of static charge and hence reduce the likelihood of the particles becoming trapped between the piston rings and the optical barrel, thereby damaging the barrel or leading to a catastrophic failure of the engine. The seed density was therefore controlled leading to approximately 3–4 particles per interrogation region of 16×16 pixels.

3 High-Speed Spray Imaging

To understand the temporal development of a GDI spray requires imaging along multiple planes to include data from the 3 orthogonal axes. With the laser sheet along the spray axis the penetration of the spray as a function of time and the spray cone angle may be measured, see Fig. 2. In this figure, images are shown at a temporal resolution of 5 crank angle degrees (CAD) and from two engine runs: the first using a lens F# of 5.6 in order to show the early spray propagation where the spray is dense and the second with an F# of 2.8 to bring out the sparse liquid spray detail towards the end of the compression stroke. The early images, up to 70 CAD before top dead centre (BTDC) at the end of the compression stroke, show both the main spray on the right-hand side coming from the injector at the upper right of each image and a reflection of the spray from the inside left surface of the optical barrel. In the early stage of injection the prespray may be observed (at 90 and 85 CAD BTDC). The main spray appears to slow from 85 to 75 CAD BTDC; high-speed imaging on a plane orthogonal to the main spray propagation direction reveals that the spray is in fact moving rapidly away from the original spray axis as it is

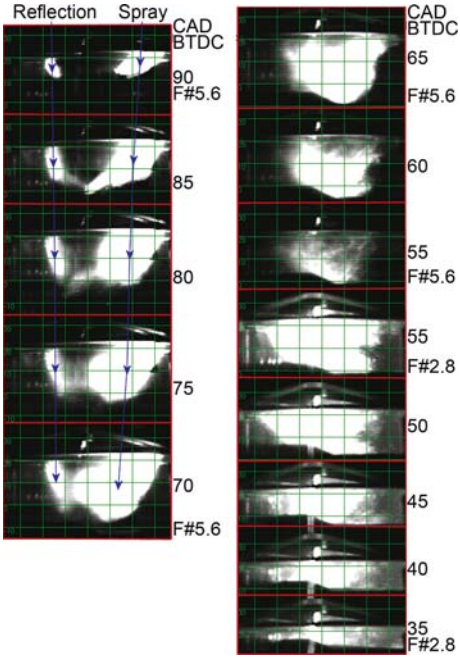

Fig. 2. Temporal development of a GDI spray imaged along the centerline of the injector, start of injection 95 CAD BTDC compression stroke. The images are at 5 CAD intervals, from 90 to 55 CAD BTDC at a lens F# of 5.6 and from 55 to 35 CAD BTDC at an F# of 2.8

influenced by the in-cylinder axial swirl generated at the intake ports. The change in lens F# allows the remaining liquid-phase fuel to be imaged up to the typical ignition timing at 30–35 CAD BTDC and the fuel cloud is seen to reside centrally beneath the spark plug in an ideal location for ignition. The spark plug can be identified as an increasingly bright region directly above the head-gasket plane.

Imaging in a vertical plane (see Fig. 1) orthogonal to the main spray propagation direction reveals the affect of axial swirl on spray location, see Fig. 3. The left-hand side of Fig. 3 shows the temporal development of the spray with maximum axial swirl ratio (2.8) and at an engine speed of 2000 rpm. It can clearly be seen that the spray arrives left of center with part of the spray falling to the left of the piston bowl. In contrast, at the maximum axial swirl ratio minus 40 % the spray propagation is initially more central and is contained within the piston bowl, thereby maintaining the location of the fuel cloud with respect to the spark plug. These results are consistent with the operation of a thermodynamic engine with the same geometry; at maximum axial swirl significantly higher hydrocarbon emissions were produced compared to those with 40 % less axial swirl ratio. It should be noted that Figs. 2 and 3 refer to different cylinder-head and piston-crown geometries.

Spray imaging by Mie scattering is also useful in identifying problem areas when a GDI spray is introduced during the induction stroke for engine operation with a homogeneous fuel–air mixture. Figure 4 shows the view

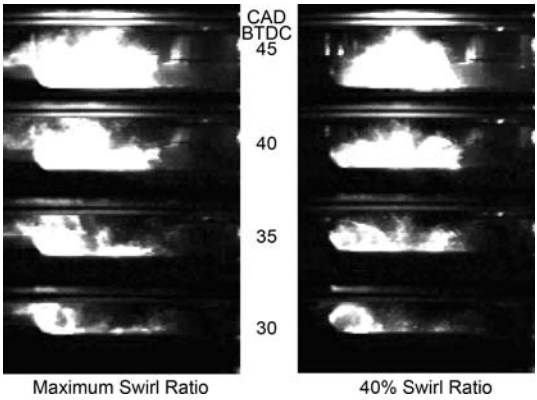

Fig. 3. GDI spray arrival in the piston bowl for maximum and 40 % axial swirl levels, the imaged plane is orthogonal to the direction of spray propagation. The images are at 5 CAD intervals

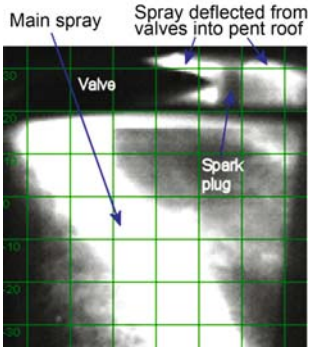

Fig. 4. GDI spray following injection on the induction stroke for homogeneous engine operation with the start of injection at 60 CAD ATDC at the beginning of the induction stroke and the image is shown at 75 CAD ATDC

along the bore and spray centerline where the inlet valves are open and the main spray can be seen to propagate below the valves. In this case, the start of injection was set at 60 CAD after top dead center (ATDC) at the beginning of the induction stroke, and the image is shown at 75 CAD ATDC. However, parts of the spray impinge on the back of the valves, and are deflected up into the head of the engine wetting the spark plug and the exhaust valves, again leading to poor hydrocarbon emission performance and potential ignition problems. Note that Fig. 4 was recorded from the opposite side of the engine compared to Fig. 2, hence the spray is seen to derive from the top left of the image.

3.1 Statistical Analysis of Cyclic Repeatability of Spray Propagation

A more detailed analysis of the spray under the influence of various experimental parameters, e.g., start of injection (SOI) timing, injection duration and in-cylinder flow swirl, can be made using a statistical analysis. A preprocessing stage may be performed by capturing an image sequence without the spray and this sequence subtracted from each cycle of spray images. Then, a threshold operation is performed to identify pixels where fuel is present. An adaptive approach to threshold selection is to calculate the grayscale corresponding to the image background, I_b, e.g., from the peak of an image histogram, and then using the measured maximum intensity, I_Max, the threshold is found as: $I_\mathrm{t} = I_\mathrm{b} + p(I_\mathrm{Max} - I_\mathrm{b})$ where p is a percentage. The most stable results have been found using $p = 10\,\%$. This operation is performed on each image in a sequence from a single injection event and repeated for many engine cycles. A new binary image sequence is generated where each pixel is white when:

$$\frac{\sum_{i=1}^{n}[IF(I(x,y,t,i) > I_\mathrm{t}) = 1,\ \mathrm{ELSE}\ 0]}{n} > \mathrm{PR}\,,$$

where (x, y) refer to a particular pixel, t is the time within an engine cycle normally expressed in CAD, i is the cycle number, n is the number of cycles of data obtained and PR is a defined probability. Most important to the development of the combustion system is to know where fuel is always present, i.e., to obtain the image sequence with PR = 1. A representative set of results are summarized in Fig. 5 obtained from a plane parallel and just beneath the head gasket. Each row of the image corresponds to images at a particular crank angle. The columns are for a particular probability, from the left, PR = 0.5, 0.8, 1. The variability in the spray field can be seen between the columns where towards the end of the compression stroke the size of the fuel cloud with PR = 0.5 is significantly larger than that with PR = 1. The data may be reduced further to extract the distance between the center of the fuel cloud and the spark plug for a particular probability as a means of comparing different engine configurations. Four engine setups are compared in this way in Fig. 6 with PR = 1. Clear differences can be observed between the different configurations. The data show that the optimum configurations are with maximum swirl and an early start of injection (97 CAD BTDC) and with 40 % less swirl and later injection (73 CAD BTDC). Further data, similar to Fig. 3, showed that with early injection some of the fuel was lost outside the piston bowl. Hence, from a combination of the statistical analysis and the high-speed image sequences the optimum configurations can be determined.

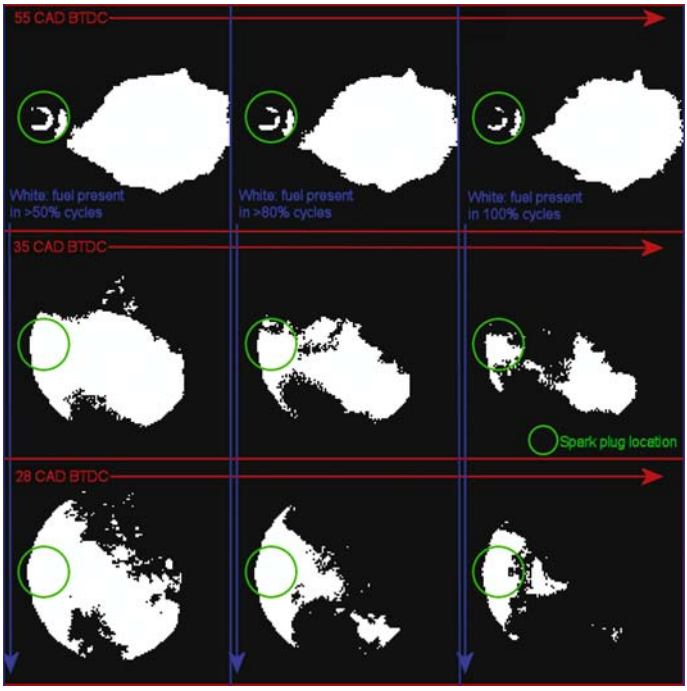

Fig. 5. Binary images showing the probability of fuel presence and resolved through the injection cycle

4 High-Speed PIV

The high-speed, temporally resolved particle images are processed to obtain the corresponding velocity vector fields using a normalized cross covariance correlation algorithm [11]. The analysis is problematic owing to the low seeding density that must be used for compatibility with the optical engine and that the analysis must be fully automated owing to the large quantity of vector maps that must be obtained in order to determine cyclic variability – vector fields resolved at 1 CAD resolution in many engine cycles. To improve the reliability of the cycle-resolved vector fields the product of crosscorrelation functions from consecutive image pairs is determined for each interrogation region [7]. For the particular results shown here, temporal sequences of 4 crosscorrelation functions were found to be optimal, representing a compromise between improved signal-to-noise ratio and the average timescale for flow similarity. The vector fields were postprocessed using a median filter to remove outliers, with 2nd or 3rd peak vectors substituted if appropriate and based on the fit with the surrounding vectors. It is estimated that some outlier vectors remained at the edge of the measurement field after the postprocessing operations and could be observed in $\sim 10\,\%$ of the vector maps in any engine cycle.

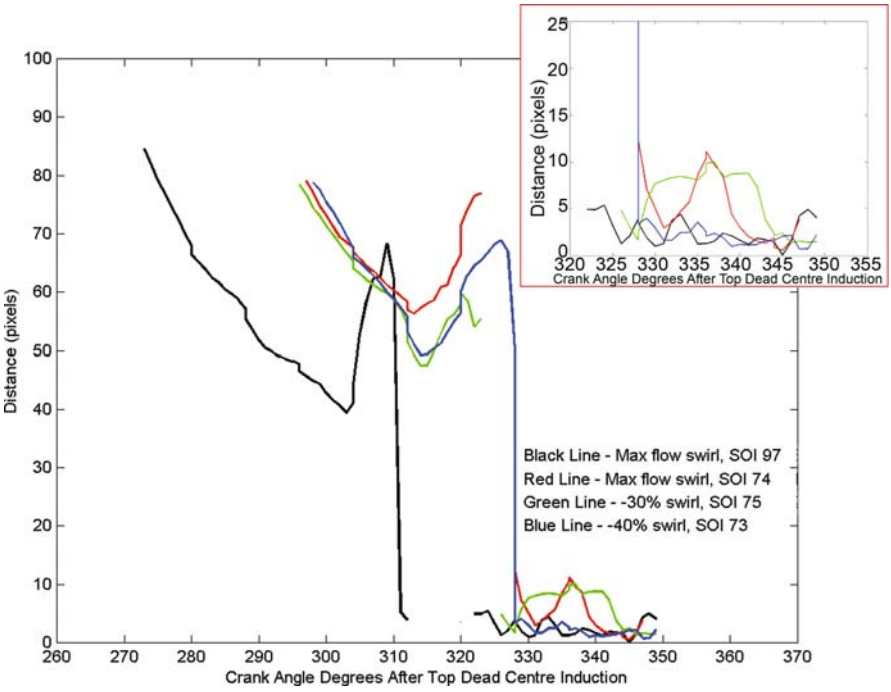

Fig. 6. Distance of fuel cloud from the spark plug for 4 engine configurations, *inset:* detail at the end of the compression stroke

4.1 Cyclic Variability Analysis of Temporally Resolved PIV Data

The meaning of cyclic variability is illustrated in Fig. 7. At each interrogation region a temporally resolved velocity is obtained and is shown schematically as the black line in Fig. 7. This velocity can be thought of as being made up of a number of components: a velocity that represents the average over all engine cycles, a term for the cyclic variability and a term for flow turbulence. The flow turbulence can be considered to be a high-frequency fluctuation and hence may be removed using appropriate temporal or Fourier-domain filtering resulting in a single cycle mean velocity at that point, shown as the red line in Fig. 7 [1]. By taking the average of the single cycle mean velocities over a representative number of engine cycles gives the ensemble mean velocity at the point, shown as the blue line in Fig. 7. The difference between the ensemble and single cycle means gives the cyclic variability for that particular engine cycle; graphically this is the difference between the red and blue lines in Fig. 7. To obtain a statistically representative value the individual cyclic variability values are averaged over a number of cycles to generate a scalar result at each interrogation region and resolved through time.

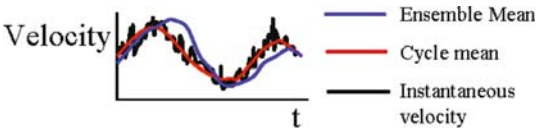

Fig. 7. Illustration of the ensemble-average velocity, the single cycle mean velocity and the instantaneous velocity from a single cycle

In this work the measured temporally resolved velocity at each interrogation region has been lowpass filtered in the temporal domain with a cutoff frequency at $\sim$ 300 Hz. This particular cutoff frequency was selected such that the smallest resolvable eddies would be removed [7]. The removal of the turbulence component was found to also remove most of the remaining outlier vectors as the outliers were typically present in single vector maps. Therefore, the outliers do not contribute to the calculated cyclic variability measure.

4.2 Results

The data presented were obtained at an engine speed of 2000 rpm, using a prototype cylinder head and piston crown that were practically identical in geometry to those being used in thermodynamic engine tests. By means of a butterfly valve in one of the two inlet port tracts, the in-cylinder axial swirl level could be varied. Two settings were evaluated, referred to as A and B, corresponding to maximum axial swirl and a medium level. Representative data from a single engine cycle during the compression stroke is shown in Fig. 8. The images show the temporal flow development in 5 CAD increments from 260 to 315 CAD BTDC. It can be seen that there is excellent spatial consistency across the vector fields. Regions of high-velocity tend to occur because of locally high-velocity jets of air that are moving through the measurement plane.

To summarize the results of the statistical analysis, Fig. 9 shows the ensemble-average vector fields at crank angles of 275 and 300° BTDC and the scalar average cyclic variability distributions at the same crank angles for engine configurations A and B. It can be seen that the cyclic variability maps also show good spatial consistency, indicating that the dominant variability effects occur in specific areas that are larger than the interrogation regions. Fifteen engine cycles of data were used for the analysis for each engine configuration. Whilst this number of cycles is relatively low, it has been identified that the mean flow velocity after 15 cycles at any particular location remains within $1\,\mathrm{m\,s^{-1}}$ of that evaluated from the first 10 engine cycles. Therefore, the ensemble-averaged velocity field has been determined to an uncertainty of $1\,\mathrm{m\,s^{-1}}$. In contrast, the scalar cyclic variability maps show peak values in excess of $4\,\mathrm{m\,s^{-1}}$ and hence the cyclic variability data is statistically relevant even though the number of cycles analyzed is comparatively low.

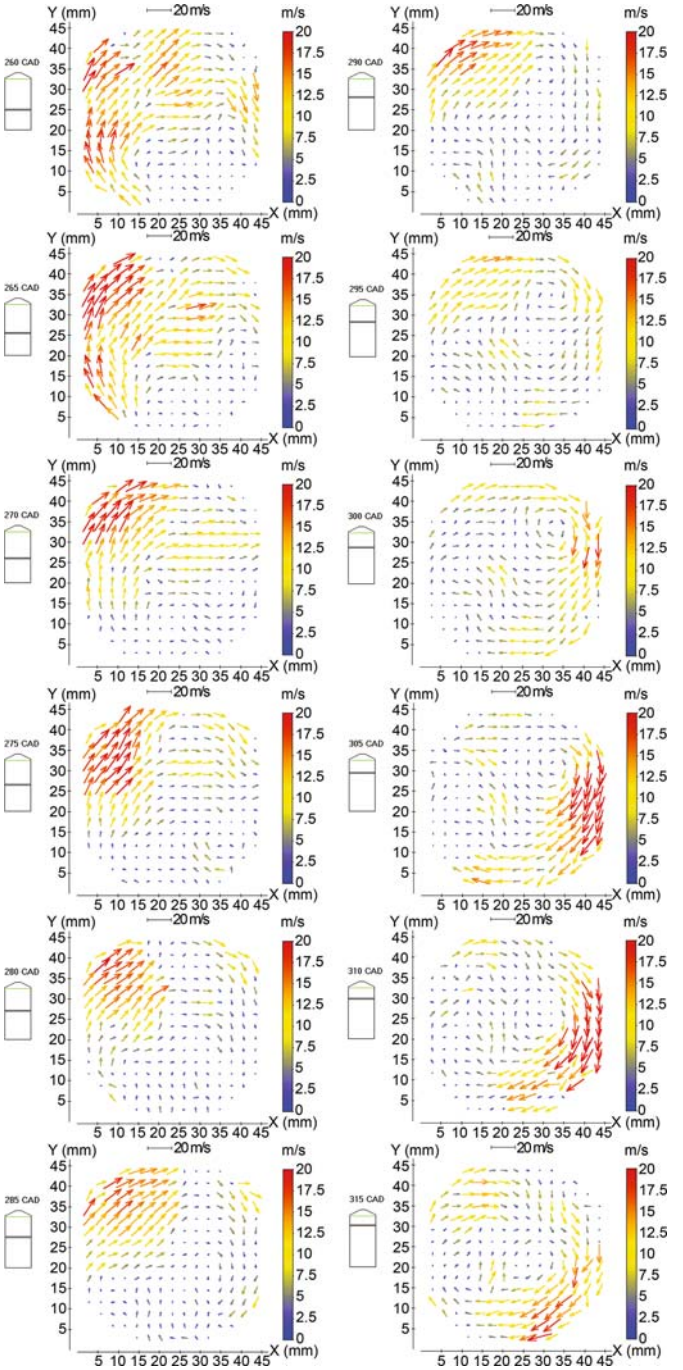

Fig. 8. Vector fields at 5 CAD increments from a single engine cycle for engine configuration B

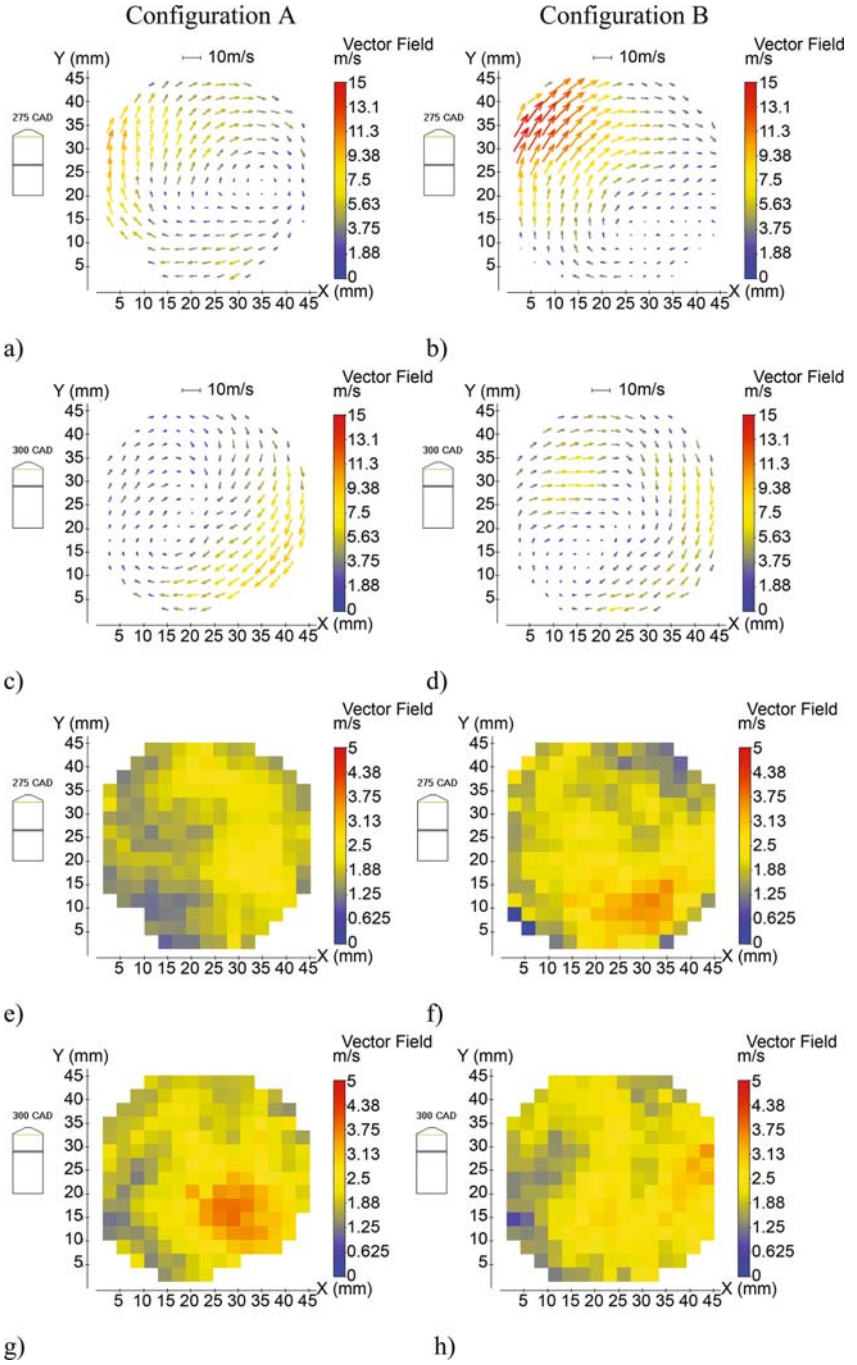

Fig. 9. Vector fields, (**a**–**d**), and cyclic variability distributions, (**e**–**h**), for 2 crank angles, 275 and 300 BTDC, and for engine configurations A and B

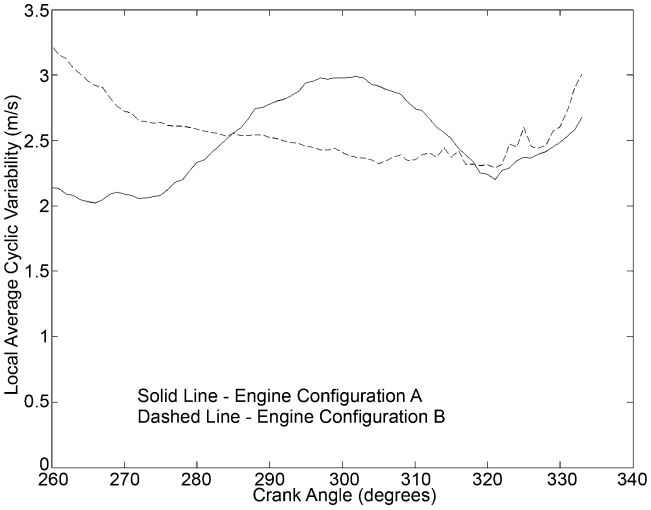

Fig. 10. Average cyclic variability across the region that most affects spray transport for engine configurations A and B

The data show interesting trends between the two engine configurations. There are increased levels of cyclic variability in the lower right of the distributions in Figs. 9f,g corresponding to 275 CAD BTDC with configuration B and 300 CAD BTDC with configuration A. Therefore, the cyclic variability is seen to peak at different points in the engine cycle for the two configurations. Given that a typical start of injection timing for the spray occurs around 290 CAD BTDC and that the spray propagates directly into the region of higher cyclic variability, it would be expected that configuration B would lead to less variability in spray transport than configuration A. Furthermore, when looking at the ensemble mean vector field for configuration B at 300 CAD BTDC it can be seen that the flow speed is considerably lower than for configuration A and hence the spray is less likely to be shifted away from the center of the combustion chamber for configuration B. These two effects combine to give a combustion system that is expected to give greater reliability in configuration B. Indeed, this conclusion has been borne out in the results of thermodynamic engine testing where the covariance of the indicated mean effective pressure (IMEP) – a value representing how smooth the engine is operating – shows lower levels of variability for configuration B than for configuration A. The cyclic variability data may be reduced to a single line graph for comparison of the two configurations by taking a mean value of variability over the region that most affects spray transport. The result for configurations A and B is shown in Fig. 10 and exhibits the same trends as have been described above.

5 Future Prospects in High-Speed PIV

Since the time when these experiments were performed there have been significant developments in both laser and camera hardware for time-resolved measurements. For example, dual-cavity solid-state lasers offering $> 10\,\text{kHz}$ repetition rate are now commercially available. Such systems offer considerable advantages over the use of a single copper-vapour laser in that the pulse separation for crosscorrelation analysis is then independent of the pulse repetition rate. Hence, higher flow velocities could be measured and hence a more complete analysis of the full induction and compression stroke could be performed. Furthermore, the beam quality is considerably higher from a solid-state laser allowing the generation of thinner lightsheets with greater energy density. Therefore, the use of more conventional oil-drop seeding (rather than large hollow microspheres) is expected to be successful leading to the potential of extracting the per-cycle flow turbulence in addition to the variability. Similar developments have taken place in high framing rate digital cameras. The Kodak4540 system used in this work has a pixel clock of 200 MHz, whereas modern cameras offer over 10 times this value, to 3 GHz, giving a 512×512 pixel image at 10 kHz framing rate. The increased spatial resolution can be used to give a greater number of interrogation regions and hence vectors within the measurements produced. At the same time, more sophisticated optical systems are being developed for 3D particle metrology from a single view [12] or using multiple views [13] that ultimately offer the potential for genuinely 4D quantitative measurements in such systems. The increased capability of new high-speed PIV hardware will also enable measurements of flow variability in the presence of the directly injected spray, thereby enabling the influence of the spray on the mean and variability of the flow field to be determined.

6 Conclusions

In this chapter, the use of high-speed, or temporally resolved imaging for the analysis of in-cylinder sprays and flows in internal combustion engines has been presented. The benefit of having the temporally resolved image sequence has been exploited in order to obtain a statistical analysis of both the spray development and vector-field variability. Furthermore, it has been shown that by suitable data analysis full-field spray and velocity data can be reduced to the temporal variation of a single parameter in order to quantify the essential characteristics of the combustion system and hence enable engineering decisions to be made.

The hardware available at the time of these experiments led to the requirement for specialized data-processing algorithms in order to reliably and automatically quantify the vector fields. To a large extent these difficulties may now be overcome using state-of-the-art lasers and cameras. Therefore, it

is expected that temporally resolved PIV and the analysis of nonrepeatable cyclic phenomena or genuinely transient behavior in spray and flow systems should become more widespread.

References

[1] J. B. Heywood: Fluid motion within the cylinder of internal combustion engines – the 1986 Freeman scholar lecture, Trans. ASME, J. Fluids Eng. p. 109 (1987) 345, 346, 354

[2] C. Arcoumanis, J. H. Whitelaw: Fluid mechanics of internal combustion engines - a review, in *Proc. Instn. Mech. Engrs.* (1987) pp. 201, C1 345

[3] D. L. Reuss, R. J. Adrian, C. C. Landreth, D. T. French, T. D. Fansler: Instantaneous planar measurements of velocity and large-scale vorticity and strain rate in an engine using particle image velocimetrypaper, in *SAE Cong. and Exposition* (1989) paper # 890616 346

[4] M. Reeves, C. P. Garner, J. C. Dent, N. A. Halliwell: Study of barrel swirl in a four valve optical I.C. engine using particle image velocimetry, in *Proc. 3rd Int. Symp. on Diagnostics and Modelling of Combustion in Internal Combustion Engines* (1994) pp. 426–436 346

[5] W.-C. Choi, Y. G. Guezennec: Measurement of cycle-to-cycle variations and cycle-resolved turbulence in an IC engine using a 3-D particle tracking velocimetry, JSME Int. J. B **41**, 991–1003 (1998) 347

[6] P. Druault, P. Guibert, F. Alizon: Use of proper orthogonal decomposition for time interpolation from PIV data, application to the cycle-to-cycle variation analysis of in-cylinder engine flows, Exp. Fluids **39**, 1009–1023 (2005) 347

[7] D. P. Towers, C. E. Towers: Cyclic variability measurements of in-cylinder engine flows using high speed particle image velocimetry, Meas. Sci. Technol. **15**, 1917–1925 (2004) 347, 353, 355

[8] R. G. Keane, R. J. Adrian: Theory of cross-correlation analysis of PIV images., Appl. Sci. Res. **49**, 191–215 (1992) 348

[9] Boud Minerals & Polymers: (2004) URL: `http://www.boud.com/expancel.htm` 349

[10] A. Melling: Tracer particles and seeding for particle image velocimetry, Meas. Sci. Technol. **8**, 1406–1416 (1997) 349

[11] H. Huang, D. Dabiri, M. Gharib: On errors of digital particle image velocimetry, Meas. Sci. Technol. **8**, 1427–1440 (1997) 353

[12] C. E. Towers, D. P. Towers, H. I. Campbell, S. J. Zhang, A. H. Greenaway: Three-dimensional particle imaging by wavefront sensing, Opt. Lett. **31**, 1220–1222 (2006) 359

[13] G. Elsinga, F. Scarano, B. Wieneke, B. W. van Oudheusden: Tomographic particle image velocimetry, Exp. Fluids **41**, 933–947 (2006) 359

Index